ADVANCED OPTICAL MATERIALS
www.advopticalmat.de

Tunable Bound States in the Continuum in a Reconfigurable Terahertz Metamaterial

Yuwei Huang, Kelson Kaj, Chunxu Chen, Zhiwei Yang, Richard D. Averitt, and Xin Zhang**

Bound states in the continuum (BIC) is an exotic concept describing systems without radiative loss. BICs are widely investigated in optics due to numerous potential applications including lasing, sensing, and filtering, among others. This study introduces a structurally tunable BIC terahertz metamaterial fabricated using micromachining and experimentally characterized using terahertz time domain spectroscopy. Control of the bending angle of the metamaterial by thermal actuation modifies the capacitance enabling tuning from a quasi-BIC state with a quality factor of 26 to the BIC state. The dynamic response from the quasi-BIC state to the BIC state is achieved by blueshifting the resonant frequency of the LC mode while maintaining a constant resonant frequency for the dipole mode. Additional insight into the tunable electromagnetic response is obtained using temporal coupled mode theory (CMT). The results reveal the effectiveness of bi-layer cantilever-based structures to realize tunable BIC metamaterials with potential applications for nonlinear optics and light-matter control at terahertz frequencies.

1. Introduction

Waves that are partially or completely confined are unique in nature. The ability to control the confinement is of significant interest due to the functionality that enables in devices such as lasers,[1–4] sensors,[5,6] filters,[7] and associated applications that include harmonic generation,[8,9] and dynamic nonlinear imaging.[10] Conventionally, a wave is confined in a Hermitian system due to the oscillation frequency being outside the continuum, which eliminates pathways for radiative energy loss. Bound states in the continuum (BIC) presents an exception where the oscillation frequency lies inside the continuum but nonetheless remains completely confined without radiative loss.[11,12] Initially proposed by von Neumann and Wigner in 1929, BICs have since been investigated in acoustic, electromagnetic, and water waves, etc.[13–18] In photonics, BICs have been realized in various structures, including gratings, waveguides, photonic crystals, and metasurfaces.[19–27]

BICs can be generally achieved through i) symmetry-protection or ii) parameter tuning. For symmetry-protected BIC structures, the bound state and continuum have distinct symmetries and thus do not couple[28,29] while parameter-tuned BIC structures have two (or more) modes where interference prevents radiative loss.[30] The most common parameter tuned (sometimes termed "accidental") BIC structures are the Fabry-Perót BIC (FP-BIC)[31,32] and the Friedrich-Wintgen BIC (FW-BIC).[33,34] The FP-BIC describes two identical resonances of two interacting cavities coupled through a single radiative channel, while the FW-BIC corresponds to two distinct resonances within the same cavity.

Metamaterials (MMs) provide an efficient approach to manipulate electromagnetic waves using artificial structures which includes creating BIC devices.[35] Indeed, BIC MMs have been investigated in several configurations.[8,28,29,36–39] However, the majority of BIC MMs that have been investigated are static. To fully realize the potential of BIC structures to create functional devices, it is important to investigate approaches that enable tuning and control. Fortunately, a raft of possibilities to realize tunable MMs have been developed including electrical, magnetic, thermal, and optical stimuli.[40–46] This, in turn, provides pathways to create reconfigurable BIC MMs.

In this work, we describe and experimentally demonstrate a microelectromechanical (MEMS)-based BIC metamaterial (BIC-MM) at terahertz frequencies. Our BIC-MM structure is based on our previous work to realize a static BIC-MM.[47] In this work, we adapt this structure using MEMS-based fabrication to construct a bi-layer cantilever structure that can be thermally manipulated.[48] Our results demonstrate tuning of the response from the quasi-BIC state to the BIC state through MEMS-based capacitive control of the BIC-MM electromagnetic response.

2. Design and Simulation

The design of our reconfigurable BIC-MMs is shown in **Figure 1**. The structure consists of two layers: a SiN_x layer (gray, bottom)

Y. Huang, C. Chen, Z. Yang, X. Zhang
Department of Mechanical Engineering and Division of Materials Science and Engineering
Boston University
Boston, Massachusetts 02215, USA
E-mail: xinz@bu.edu
K. Kaj, R. D. Averitt
Department of Physics
University of California
San Diego, La Jolla, California 92093, USA
E-mail: raveritt@ucsd.edu

The ORCID identification number(s) for the author(s) of this article can be found under https://doi.org/10.1002/adom.202300559

DOI: 10.1002/adom.202300559

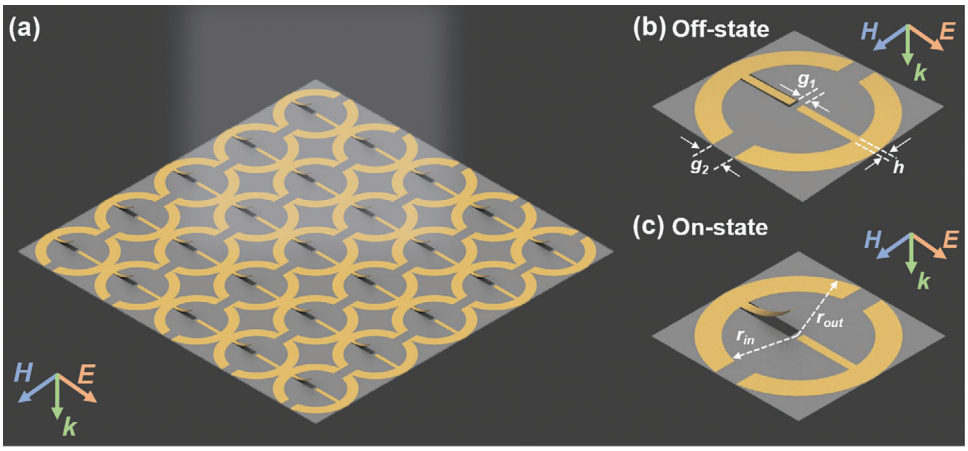

Figure 1. a) Illustrative schematic of the reconfigurable BIC metamaterials. Unit cells depicting the b) off-state and c) on-state. The dimensions of the BIC-MM are given in the main text.

and a gold MM layer (yellow, top). This structure is inspired by a high-Q anapole microwave metamaterial[49] and is redesigned for the resonances to be in the terahertz range when fabricated on a SiN_x film. The gold MM layer is 100 nm thick while the SiN_x is 400 nm thick. The overall periodicity of the top MMs is 196 μm × 196 μm. The outer radius of the ring r_{out} = 100 μm while the inner radius r_{in} = 74 μm. The width of the two middle bars is h = 12 μm and the capacitive gap between bars is g_1 = 4 μm while the outer capacitive gap between the two semi-rings is g_2 = 28 μm, as shown in **Figure 2**b. The underlying SiN_x film was etched along the three sides of one middle bar such that the middle bar can be bent out of the plane under rapid thermal annealing (RTA) process, as shown in Figure 1b,c.

The simulated transmission spectra of the reconfigurable BIC-MMs for different bending angles of the center bar are shown in Figure 2a. For the simulations the SiN_x is modeled as a lossless dielectric with permittivity ε = 7 while the gold conductivity is 4.56 × 10^7 Sm^{-1} for the metamaterial layer. Details of the simulation can be found in the Experimental section. The polarization direction of the terahertz beam (at normal incidence) is along the length of the middle bar (see the orange arrow in the inset of Figure 1). When the BIC-MM is in the off-state (i.e., zero bending angle), there are two resonant frequencies at ≈0.66 THz (orange arrow) and ≈0.88 THz (green arrow), as shown by the purple line in Figure 2a. These two modes correspond to the LC mode (0.66 THz) and the dipole mode (0.88 THz) with the surface current schematically indicated by the orange arrows and green arrows in Figure 2b,c, respectively (the simulated surface current distributions for the two modes are shown in **Figure 3**a,b). The interference between these two modes gives rise to a transmission peak at 0.69 THz (purple line in Figure 2a). This corresponds to a Friedrich-Wintgen (FW) quasi-BIC state with a Q factor of 26 (verified using coupled mode theory (CMT) below). The BIC-MM can also be tuned to the on-state, where one of the central bars is tilted out of plane (Figure 1c). With an increase of bending

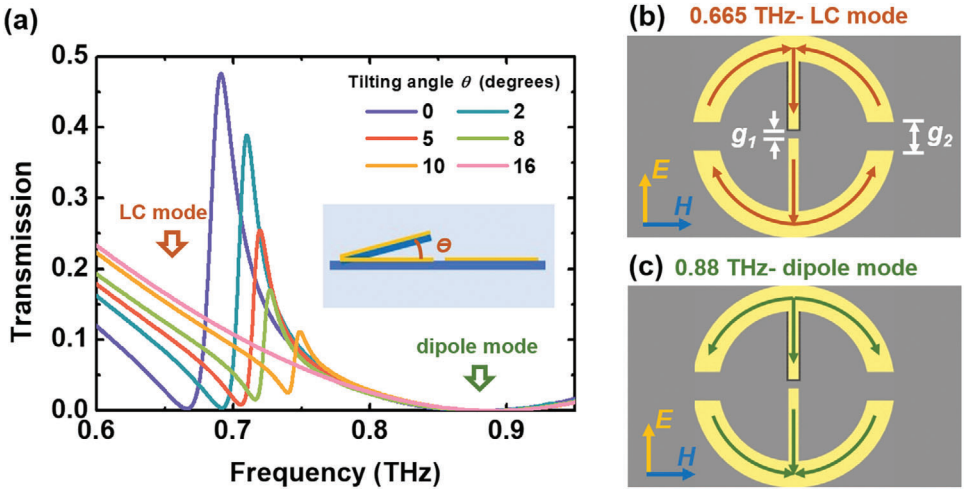

Figure 2. a) Simulated transmission spectra for different bending angles. For zero tilting angle (purple curve) the LC mode is at 0.665 THz (orange hollow arrow) and the dipole mode is at 0.88 THz (green hollow arrow). b,c) schematically show the surface current for the two mode as indicated by the arrows. The actual simulated surface current distributions can be found in Figure 3a,b).

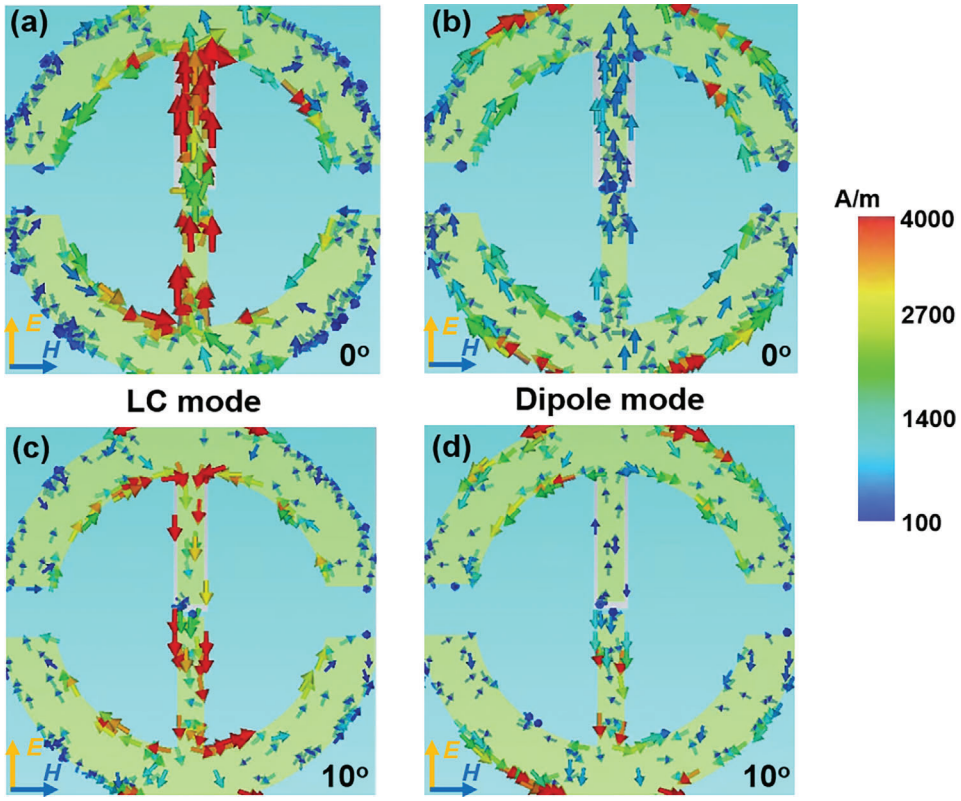

Figure 3. Surface current distributions at two mode frequencies with different bending angles. a,b) are at bending angle of 0° while c,d) are at bending angle of 10°. a,c) are at the LC mode frequencies while b,d) are at the dipole mode frequencies.

angle, the LC mode continuously shifts to higher frequencies. Correspondingly, the peak in transmission blueshifts and decreases in amplitude. For a bending angle of 16°, the transmission peak disappears, as shown by the pink line in Figure 2a. The absence of the transmission peak is indicative of the structure reaching the BIC state, as will be confirmed by CMT calculations in Section 3. It is noted that this structure achieves the BIC state when the structural symmetry is broken. This is in contrast to what would be expected for a symmetry-protected BIC, further demonstrating the accidental BIC nature of the electromagnetic response. Higher quality factors can also be achieved by adjusting the structural parameters when the structure is in the off-state, i.e., the width of the cantilever. However, there is a trade-off between the highest bending angle and the largest quality factor. To fully observe the dynamic tuning from the quasi-BIC state to BIC state, we chose the structural parameters as described in the beginning of this section.

It is interesting to understand why only the LC mode frequency blueshifts while the dipole mode frequency is constant with increased bending angle. Figure 3 shows the surface current distributions of the two modes when the bending angles are 0° and 10°, respectively. Figure 3a,c are at the LC mode frequency while Figure 3b,d are at the dipole mode frequency. From Figure 3a,b where the bending angle is 0°, the surface current is concentrated on the two central bars for the LC mode while it focuses on the two semi-rings for the dipole mode. This is also the case when the tilting angle is 10°, as shown in Figure 3c,d. As such, the LC mode frequency is more sensitive to thermal actuation, which modifies the capacitance between the two central bars when it is bent out of the plane. However, the semi-ring structure does not change, and therefore the dipole mode maintains a constant resonant frequency.

3. Results and Discussion

We fabricated the reconfigurable BIC MMs using a combination of surface and bulk-micromachining.[38] First, a 400 nm thick silicon nitride (SiN_x) film was deposited on both sides of a silicon wafer using low-pressure chemical vapor deposition (LPCVD). The SiN_x film serves as the bottom layer of this bi-layer structure. Then, the upper side of the SiN_x was intentionally etched to define the cantilever using reactive ion etching (RIE). The MMs were subsequently patterned on top of the SiN_x film with E-beam evaporation followed by lift-off in acetone. Finally, to release the bi-layer structure, the backside of the SiN_x film was selectively etched to form open windows and the entire wafer was immersed in 30% potassium hydroxide (KOH) solution to etch the silicon away. The number of unit cells of one fabricated sample is 64 × 64 with an overall area of ≈ 1.2 × 1.2 cm^2.

After we fabricated several bi-layer MM samples, rapid thermal annealing (RTA) was performed at different temperatures to obtain different bending angles of the cantilever. The bending arises from the difference of the thermal expansion coefficients between gold (14.2×10^{-6} K^{-1}) and SiN_x (2.3×10^{-6} K^{-1}). Further details of the RTA process can be found in the Experimental section. In this work, we selected 250 °C, 350 °C, and 450 °C as our

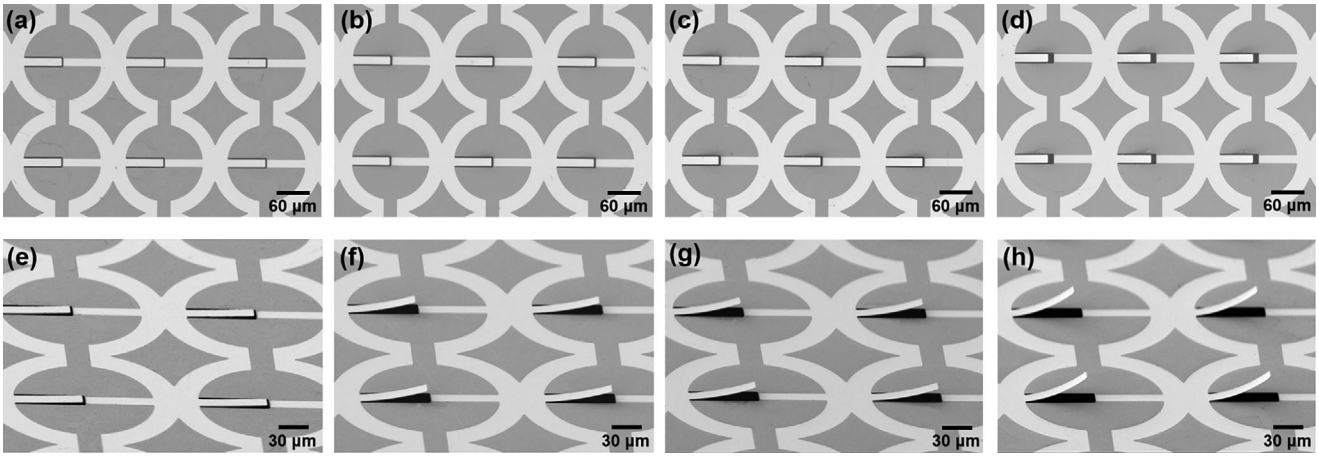

Figure 4. Scanning electron microscope (SEM) images of the fabricated samples under a,e) no RTA, b,f) RTA-250 °C, c,g) RTA-350 °C, and d,h) RTA-450 °C. a–d) are top view images and e–h) are 60° side view images.

target RTA temperatures (in addition to the pristine sample) to achieve different bending angles of the cantilever and measure the resultant terahertz responses.

Scanning electron microscope (SEM) images of the fabricated bi-layer MMs for different RTA temperatures are shown in **Figure 4**. Both the top view and the side view of the samples are included for each RTA temperature. From Figure 4a–d (or from Figure 4e–h), it is clear that the bending angle of the central bar increases with RTA temperature. Even without RTA, the cantilever is not flat with a bending angle of ≈ 2° due to residual stress. It is also noted that the cantilever exhibits a slight curvature. As the RTA temperature increases, the curvature is more obvious. In this work, we will not focus on the curvature and we will utilize "equivalent" bending angles, corresponding to the bending angles in the simulations with no cantilever curvatures that exhibit the best match with the experimental results. Since we rapidly cooled the structures to room temperature following RTA, the bending angle is maintained enabling detail terahertz measurements to be performed.

As shown in **Figure 5**, THz time-domain spectroscopy (THz-TDS) was used to measure the transmission for the fabricated samples (red dots). Details of the measurement can be found in the Experimental section. There is a blueshift of the LC mode from 0.69 THz (Figure 5a) in the pristine sample to 0.74 THz (Figure 5b) in the sample with RTA at 250 °C and further to 0.75 THz at 350 °C (Figure 5c) while the dipole mode stays at 0.9 THz. Correspondingly, the quasi-BIC transmission peak from the interference of the two modes also continuously blueshifts from 0.71 THz in the pristine sample to 0.76 THz with RTA at 350 °C. Finally, when the RTA temperature increases to 450 °C, the quasi-BIC transmission peak disappears (Figure 5d), corresponding to the BIC state. The shift of the quasi-BIC transmission peak arises from cantilever bending induced shifting of the LC mode while the dipole mode at ≈0.9 THz does not shift with the cantilever bending, as discussed above. Excellent agreement of the overall transmission is obtained between the full-wave electromagnetic simulations (blue lines) and the experimental results (red dots) in Figure 5 under different RTA temperatures corresponding to different "equivalent" bending angles. The slight deviation between the experiments and simulations arises from fabrication imperfections and measurement errors. The dashed yellow lines (which also fit the data quite well) correspond to coupled mode theory calculations that are described below.

As discussed above, the BIC-MM terahertz response arises from the interference between the LC mode and the dipole mode. As such temporal coupled mode theory (CMT) can help to understand how the transmission is modified as a function of the mode parameters. It is noted that perturbation theory is also prevalently employed to explain BIC-based responses, but it is more robust in explaining the symmetry-protected type rather than the "accidental" type, as we discussed here.[50,51] A general temporal CMT model for a system with two resonant modes coupled to two ports is[52]:

$$\frac{d}{dt}\begin{bmatrix} a_1 \\ a_2 \end{bmatrix} = (j\Omega - \Gamma)\begin{bmatrix} a_1 \\ a_2 \end{bmatrix} + K\begin{bmatrix} s_{1+} \\ s_{2+} \end{bmatrix} \tag{1}$$

$$\Omega = \begin{bmatrix} \omega_{01} & k \\ k & \omega_{02} \end{bmatrix}, \quad \Gamma = \begin{bmatrix} \gamma_1 & \gamma_{12} \\ \gamma_{12} & \gamma_2 \end{bmatrix}, \quad K = \begin{bmatrix} k_{11} & k_{12} \\ k_{21} & k_{22} \end{bmatrix} \tag{2}$$

In these equations, $[a_1, a_2]^T$ are the resonance amplitudes while ω_{01} and ω_{02} are the resonant frequencies of the two modes supported by the system. $\gamma_1 = \gamma_{r1} + \gamma_{o1}$ and $\gamma_2 = \gamma_{r2} + \gamma_{o2}$ are the damping rates of the two modes, respectively. γ_{ri} ($i = 1, 2$) is the radiative damping while γ_{oi} is the damping rate due to ohmic losses. k represents the direct coupling rate between the two modes and $\gamma_{12} = \gamma_{21} = \sqrt{\gamma_1\gamma_2}$ is the overall damping of the coupled system. k_{ij} ($i, j \in \{1, 2\}$) is the coupling coefficient between the mode i and the mode j while s_{1+} (s_{2+}) is the input wave amplitude from the port 1(2). The outgoing waves from the excited resonant modes are thus given by:

$$\begin{bmatrix} s_{1-} \\ s_{2-} \end{bmatrix} = C\begin{bmatrix} s_{1+} \\ s_{2+} \end{bmatrix} + D\begin{bmatrix} a_1 \\ a_2 \end{bmatrix} \tag{3}$$

$$C = \begin{bmatrix} r_d & t_d \\ t_d & r_d \end{bmatrix}, \quad D = \begin{bmatrix} d_{11} & d_{12} \\ d_{21} & d_{22} \end{bmatrix} \tag{4}$$

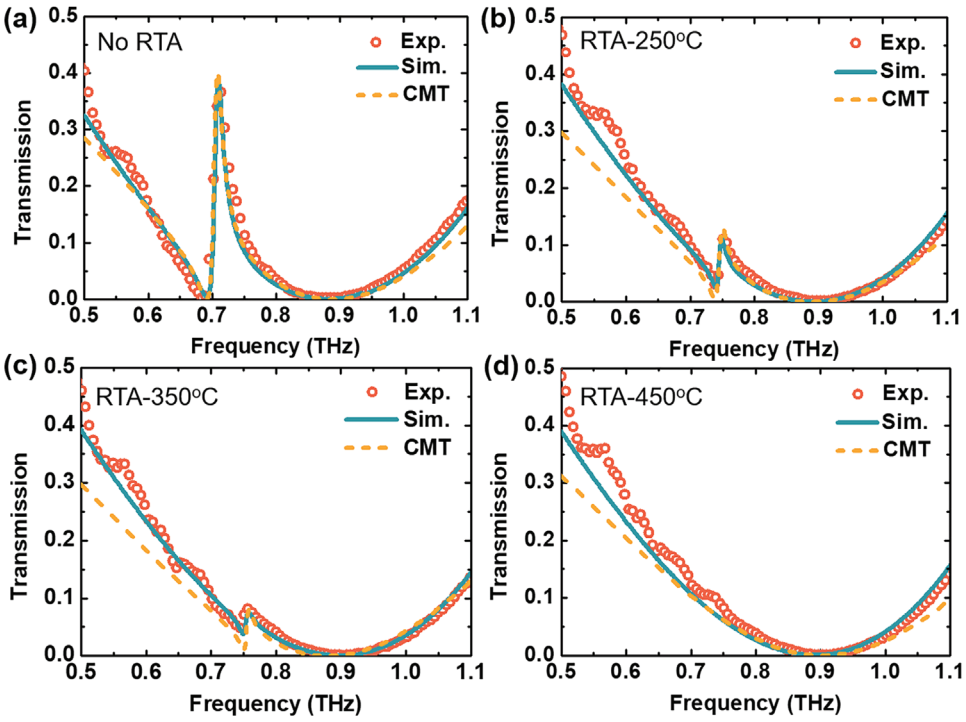

Figure 5. Comparison of the transmission spectra from experiment, FEM simulations, and CMT calculations for a) no RTA, b) RTA at 250 °C, c) RTA at 350 °C, and d) RTA at 450 °C. The red hollow dots are the experimental data, the blue lines are FEM simulations and the yellow dash lines are calculation results from CMT.

where $s_{1\_}$ ($s_{2\_}$) is the outgoing wave amplitude at port 1(2). r_d and t_d are the direct reflection and transmission coefficient between the ports without resonances. d_{ij} ($i, j \in \{1, 2\}$) is the coupling coefficient between the port j and the mode i. Based on energy conservation, $k_{11} = k_{12} = |d_{11}| = |d_{12}| = \sqrt{\gamma_1}$ and $k_{21} = k_{22} = |d_{21}| = |d_{22}| = \sqrt{\gamma_2}$.

Solving the Equations 1 and 2, yields:

$$a_1(\omega) = \frac{jk - \gamma_{12}}{j(\omega - \omega_{01}) + \gamma_1} a_2(\omega) + \frac{\gamma_1}{j(\omega - \omega_{01}) + \gamma_1} s_{1+}(\omega) \quad (5)$$

$$a_2(\omega) = \frac{(jk - \gamma_{12})\sqrt{\gamma_1} + [j(\omega - \omega_{01}) + \gamma_1]\sqrt{\gamma_2}}{[j(\omega - \omega_{02}) + \gamma_2][j(\omega - \omega_{01}) + \gamma_1] - (jk - \gamma_{12})^2} s_{1+}(\omega) \quad (6)$$

Based on Equations 3 and 4, the outgoing wave amplitude at port 2 is:

$$s_{2-}(\omega) = t_d s_{1+}(\omega) - (\sqrt{\gamma_1} a_1(\omega) + \sqrt{\gamma_2} a_2(\omega)) \quad (7)$$

Thus, the transmission coefficient can be calculated by $t_{21}(\omega) = s_{2-}(\omega)/s_{1+}(\omega)$. In a system without ohmic losses (i.e., idealized), the decay rate is fully determined by the radiative loss, i.e. $\gamma_1 = \gamma_{r1}$, $\gamma_2 = \gamma_{r2}$. The CMT calculations without ohmic loss result in unity transmission at the peak, as shown in **Figure 6**a (red line). However, more realistically, the ohmic loss from gold must be included in addition to the radiative loss (i.e., $\gamma_{o1} \neq 0$ and $\gamma_{o2} \neq 0$). The dashed blued line in Figure 6a shows the transmission with ohmic loss included. The quality factors can be expressed in terms of the decay rates as follows:

$$Q_{r1} = \omega_{01}/(2\gamma_{r1}), \quad Q_{o1} = \omega_{01}/(2\gamma_{o1}) \quad (8)$$

$$Q_{r2} = \omega_{02}/(2\gamma_{r2}), \quad Q_{o2} = \omega_{02}/(2\gamma_{o2}) \quad (9)$$

For a Friedrich-Wintgen BIC-MM, the BIC state is achieved when:

$$k(\gamma_1 - \gamma_2) = \sqrt{\gamma_1\gamma_2}(\omega_{01} - \omega_{02}) \quad (10)$$

We used the above CMT equations to fit the simulations and experimental results. To obtain the best fit of the BIC-MM transmission responses using CMT, we only increased the LC mode frequency while holding the dipole mode resonance frequency and the decay rates of both modes constant (the details of the fitting parameters are listed in **Table 1**). Figure 5 shows the comparison between the CMT calculations (yellow dashed lines) and simulation/experimental results (blue lines/red dots). We find that the CMT model with appropriate ohmic loss works well, not only for the shape of the two modes but also for the amplitude of the quasi-BIC peaks. In addition, Equation 10 is also satisfied when we further increase the LC mode frequency to fit the transmission responses for the MM sample that undergoes the RTA process at 450 °C (Figure 5d), which further verifies that it is at the BIC state.

The transmission response (from FEM simulations) as a function of bending angle is plotted in Figure 6c, showing the evolution from the quasi-BIC state to the BIC state. The transmission peak continuously blueshifts from 0.71 THz to 0.76 THz with decreased transmission amplitude when the bending angle increases and finally vanishes at 16° corresponding to the BIC

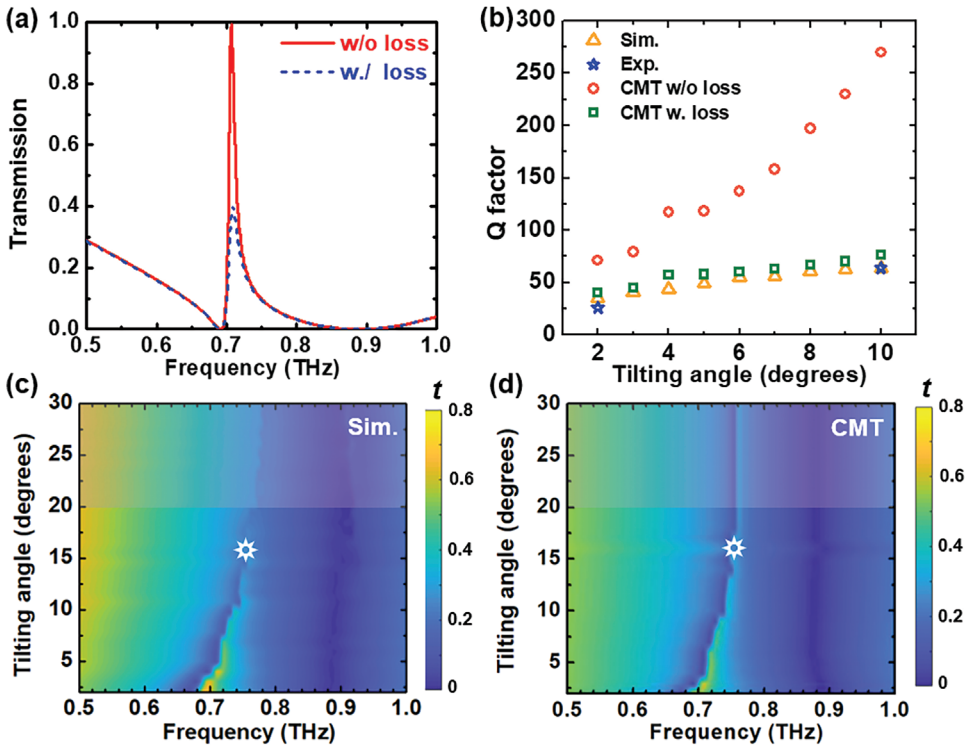

Figure 6. a) Comparison of calculated transmission spectra for BIC-MM using CMT with and without consideration of ohmic loss. b) Theoretical, simulated, and measured Q factors using Fano resonance fitting for the MMs as a function of "equivalent" tilting angles. c) Dependence of the simulated transmission spectra on tilting angles of the central bar. d) Calculated transmission spectra from CMT for different LC mode frequencies. The white stars in c,d) denote the BIC state.

state (indicated by white star on plot). We also employed our CMT modeling with ohmic losses to compare with the simulations, as shown in Figure 6d. For the CMT modeling, we only changed the LC mode frequency while maintaining the dipole mode frequency and other parameters. Good agreement for both the transmission peak frequencies and amplitudes can be found by comparing Figure 6c,d. Calculated Q factors determined from the simulations (yellow triangles), CMT modeling with ohmic loss (green squares), and experiments (blue stars) in pristine sample and at RTA 250 °C are included in Figure 6b. The Q factors are determined through fitting with a Fano resonance lineshape:

$$T = \left| a_1 + ia_2 + \frac{b}{\omega - \omega_0 + i\gamma} \right|^2 \tag{11}$$

$$Q = \frac{\omega_0}{2\gamma} \tag{12}$$

Table 1. Fitting parameters for the BIC-MMs using CMT.

RTA temperature (°C)	ω_{01} (× 2π THz)	Q_{r1}	Q_{o1}	ω_{02} (× 2π THz)	Q_{r2}	Q_{o2}	k (× 2π THz)
no RTA	0.7	2.8	150	0.88	1	70	0.04
250	0.755						
350	0.765						
450	0.835						

where T is the transmission, ω_0 is the resonance frequency, γ is the damping rate, a_1, a_2, and b are constant and Q is the quality factor.

The good agreement of the Q factors further validates our theoretical model although the Q factors cannot be calculated when the MM is close to the BIC state where the "equivalent" bending angle increases to 16° as the transmission peak amplitude gradually decreases and finally vanishes. We also include the Q factors from CMT modeling without ohmic loss in Figure 6b for reference (red dots). The Q factor almost linearly increases with the bending angle, which could potentially be achieved using lossless materials such as superconductors. Although the ohmic losses can significantly decrease both the transmission peak amplitude and the Q factors from the ideal situation (no ohmic loss), the increase of the Q factors with increased tilting angles demonstrates that the structure is approaching BIC state. It is noted that by further increasing the bending angle after our MM achieves BIC state, there is a small transmission peak occurring again at a frequency higher than 0.76 THz, as shown in gray area in Figure 6c, corresponding to quasi-BIC states again. The significantly decreased transmission amplitude is attributed to decreased intensities of both the dipole mode and LC mode since the cantilever is further deviated out of the plane. It is also noted that higher bending angles cannot be achieved due to structural limitations. Improvement can be realized by utilizing a different bottom layer material or optimizing the top MM design, but this is beyond the focus of this work.

4. Conclusion

We experimentally demonstrated a structurally tunable THz BIC metamaterial in a bi-layer structure. Temperature tuning of the bending angle of the middle bar of the metamaterial resonator modifies the coupling between the dipole mode and the LC mode. This, in turn, changes the transmission from a Fano resonance with a quality factor of 26 at the quasi-BIC state to a BIC state when the Friedrich-Wintgen condition is achieved. The tuning response and interpretation in terms of a Friedrich-Wintgen BIC are consistent with coupled mode theory calculations and full wave electromagnetic simulations. Our work demonstrates a potential method toward functional terahertz devices through the integration of metamaterials with MEMS technology for enhanced light-matter interaction and nonlinear applications.

5. Experimental Section

Simulation: The frequency domain solver in a commercial software CST microwave studio 2021 was employed for simulating the transmission of the BIC-MMs. The unit cell conditions were used for x and y directions, while the open space condition was used for the z direction. The gold for the metamaterial layer was characterized as a lossy metal with an electric conductivity of 4.56×10^7 Sm^{-1} while SiN_x was treated as a no-loss dielectric with permittivity of $\varepsilon = 7$.

Fabrication: First, 400 nm LPCVD silicon nitride (Addison Engineering, Inc.) was coated on both sides of a silicon wafer. Subsequently, the front side SiN_x was selectively etched with RIE (Plasma-Therm 790) with SF_6/He, 40 mTorr pressure, and 110 Watts RF power. Next, the 100 nm thick gold metamaterial structures were deposited with E-beam evaporation (Angstrom Engineering EVOVAC) at 1 Å·s^{-1}, followed by a lift-off process. Subsequently, the entire structure was released with KOH etching (3:5 = H_2O: 48% KOH solution) at 100 °C. Finally, RTA (Modular Process Technology RTP-600 S, at different temperatures for 10 min) on the fabricated samples was performed to achieve the desired bending angles. The RTA process consisted of three steps: first, the temperature was increased from room temperature to a target temperature within 1 min; second, the temperature was maintained for 10 min; third, the temperature was decreased to room temperature again within 1 min. Detailed fabrication process flow can be found in the Supporting Information.

Characterization: The transmission of the BIC-MMs was characterized using THz time domain spectroscopy (THz-TDS) using photoconductive antennas. The THz pulses are focused on the sample through a set of parabolic mirrors, were generated using a titanium sapphire laser at 800 nm, 20 fs and 80 MHz repetition rate. The transmitted pulses were measured with another photoconductive antenna. In the measurement, the electric field was polarized in the x-direction, as shown in Figure 1a. The temporal responses were then acquired and Fourier transformed into the frequency domain. The experiments were performed in a dry air chamber in order to avoid THz absorption by water vapor.

Supporting Information

Supporting Information is available from the Wiley Online Library or from the author.

Acknowledgements

The authors acknowledge support from National Science Foundation ECCS-1810252. Work at UCSD was supported by the Army Research Office (ARO) under Grant no. MURI W911NF-16-1-0361.

Conflict of Interest

The authors declare no conflict of interest.

Data Availability Statement

The data that support the findings of this study are available from the corresponding author upon reasonable request.

Keywords

bound states in the continuum, photonics, reconfigurable metamaterials, terahertz

Received: March 7, 2023
Revised: May 31, 2023
Published online:

[1] S. Noda, M. Yokoyama, M. Imada, A. Chutinan, M. Mochizuki, *Science* **2001**, *293*, 1123.
[2] K. Hirose, Y. Liang, Y. Kurosaka, A. Watanabe, T. Sugiyama, S. Noda, *Nat. Photonics* **2014**, *8*, 406.
[3] E. Miyai, K. Sakai, T. Okano, W. Kunishi, D. Ohnishi, S. Noda, *Nature* **2006**, *441*, 946.
[4] H. Matsubara, S. Yoshimoto, H. Saito, Y. Jianglin, Y. Tanaka, S. Noda, *Science* **2008**, *319*, 445.
[5] A. A. Yanik, A. E. Cetin, M. Huang, A. Artar, S. H. Mousavi, A. Khanikaev, J. H. Connor, G. Shvets, H. Altug, *Proc. Natl. Acad. Sci.* **2011**, *108*, 11784.
[6] B. Zhen, S. L. Chua, J. Lee, A. W. Rodriguez, X. Liang, S. G. Johnson, J. D. Joannopoulos, M. Soljačií, O. Shapira, *Proc. Natl. Acad. Sci.* **2013**, *110*, 13711.
[7] J. M. Foley, S. M. Young, J. D. Phillips, *Phys. Rev. B* **2014**, *89*, 165111.
[8] K. Koshelev, Y. Tang, K. Li, D. Y. Choi, G. Li, Y. Kivshar, *ACS Photonics* **2019**, *6*, 1639.
[9] Z. Liu, Y. Xu, Y. Lin, J. Xiang, T. Feng, Q. Cao, J. Li, S. Lan, J. Liu, *Phys. Rev. Lett.* **2019**, *123*, 253901.
[10] L. Xu, K. Zangeneh Kamali, L. Huang, M. Rahmani, A. Smirnov, *Adv. Sci.* **2019**, *6*, 1802119.
[11] C. W. Hsu, B. Zhen, A. D. Stone, J. D. Joannopoulos, M. Soljačić, *Nat. Rev. Mater.* **2016**, *1*, 16048.
[12] S. I. Azzam, A. V. Kildishev, *Adv. Opt. Mater.* **2021**, *9*, 1.
[13] E. Wigner, J. Von Neumann, *Z Phys.* **1928**, *30*, 465.
[14] Z. G. Chen, C. Xu, R. Al Jahdali, J. Mei, Y. Wu, *Phys. Rev. B* **2019**, *100*, 075120.
[15] K. Fan, I. V. Shadrivov, W. J. Padilla, *Optica* **2019**, *6*, 169.
[16] S. Han, P. Pitchappa, W. Wang, Y. K. Srivastava, M. V. Rybin, R. Singh, *Adv. Opt. Mater.* **2021**, *9*, 2002001.
[17] P. J. Cobelli, V. Pagneux, A. Maurel, P. Petitjeans, *Europhys. Lett.* **2009**, *88*, 20006.
[18] P. J. Cobelli, V. Pagneux, A. Maurel, P. Petitjeans, *J. Fluid Mech.* **2011**, *666*, 445.
[19] C. W. Hsu, B. Zhen, J. Lee, S. L. Chua, S. G. Johnson, J. D. Joannopoulos, M. Soljačić, *Nature* **2013**, *499*, 188.
[20] S. I. Azzam, V. M. Shalaev, A. Boltasseva, A. V. Kildishev, *Phys. Rev. Lett.* **2018**, *121*, 253901.
[21] S. Weimann, Y. Xu, R. Keil, A. E. Miroshnichenko, A. Tünnermann, S. Nolte, A. A. Sukhorukov, A. Szameit, Y. S. Kivshar, *Phys. Rev. Lett.* **2013**, *111*, 240403.
[22] A. Kodigala, T. Lepetit, Q. Gu, B. Bahari, Y. Fainman, B. Kanté, *Nature* **2017**, *541*, 196.

[23] L. Li, J. Zhang, C. Wang, N. Zheng, H. Yin, *Phys. Rev. A* **2017**, *96*, 13801.
[24] J. Gomis-Bresco, D. Artigas, L. Torner, *Nat. Photonics* **2017**, *11*, 232.
[25] K. Koshelev, S. Lepeshov, M. Liu, A. Bogdanov, Y. Kivshar, *Phys. Rev. Lett.* **2018**, *121*, 193903.
[26] Y. He, G. Guo, T. Feng, Y. Xu, A. E. Miroshnichenko, *Phys. Rev. B* **2018**, *98*, 161112.
[27] Y. Liang, K. Koshelev, F. Zhang, H. Lin, S. Lin, J. Wu, B. Jia, Y. Kivshar, *Nano Lett.* **2020**, *20*, 6351.
[28] L. Cong, R. Singh, *Adv. Opt. Mater.* **2019**, *7*, 1900383.
[29] S. Li, C. Zhou, T. Liu, S. Xiao, *Phys. Rev. A* **2019**, *100*, 063803.
[30] M. S. Sidorenko, O. N. Sergaeva, Z. F. Sadrieva, C. Roques-Carmes, P. S. Muraev, D. N. Maksimov, A. A. Bogdanov, *Phys. Rev. Appl.* **2021**, *15*, 034041.
[31] Z. Gong, J. Serafini, F. Yang, S. Preble, J. Yao, *Phys. Rev. Appl.* **2021**, *16*, 024059.
[32] L. L. Doskolovich, E. A. Bezus, D. A. Bykov, *Photonics Res.* **2019**, *7*, 1314.
[33] S. I. Azzam, V. M. Shalaev, A. Boltasseva, A. V. Kildishev, *Phys. Rev. Lett.* **2018**, *121*, 253901.
[34] H. M. Doeleman, F. Monticone, W. den Hollander, A. Alú, A. F. Koenderink, *Nat. Photonics* **2018**, *12*, 397.
[35] K. Koshelev, A. Bogdanov, Y. Kivshar, *Sci. Bulletin* **2019**, *64*, 836.
[36] T. C. Tan, E. Plum, R. Singh, *Adv. Opt. Mater.* **2020**, *8*, 1901572.
[37] J. Li, J. Li, C. Zheng, Z. Yue, S. Wang, M. Li, H. Zhao, Y. Zhang, J. Yao, *Carbon* **2021**, *182*, 506.
[38] H. H. Hsiao, Y. C. Hsu, A. Y. Liu, J. C. Hsieh, Y. H. Lin, *Adv. Opt. Mater.* **2022**, *10*, 2200812.
[39] X. Zhang, W. Shi, J. Gu, L. Cong, X. Chen, K. Wang, Q. Xu, J. Han, W. Zhang, *Opt. Express* **2022**, *30*, 29088.
[40] C. Chen, K. Kaj, X. Zhao, Y. Huang, R. D. Averitt, X. Zhang, *Optica* **2022**, *9*, 17.
[41] C. Chen, K. Kaj, Y. Huang, X. Zhao, R. D. Averitt, X. Zhang, *Adv. Opt. Mater.* **2021**, *9*, 2101215.
[42] X. Zhao, J. Schalch, J. Zhang, H. R. Seren, G. Duan, R. D. Averitt, X. Zhang, *Optica* **2018**, *5*, 303.
[43] M. Lei, N. Feng, Q. Wang, Y. Hao, S. Huang, K. Bi, *J. Appl. Phys.* **2016**, *119*, 244504.
[44] X. Zhao, Y. Wang, J. Schalch, G. Duan, K. Cremin, J. Zhang, C. Chen, R. D. Averitt, X. Zhang, *Acs Photonics* **2019**, *6*, 830.
[45] Y. Huang, K. Kaj, C. Chen, Z. Yang, S. Ul Haque, Y. Zhang, X. Zhao, R. D. Averitt, X. Xhang, *Acs Photonics* **2022**, *9*, 1150.
[46] Y. Huang, X. Wu, J. Schalch, G. Duan, C. Chen, X. Zhao, K. Kaj, H. Zhang, E. Roman, R. D. Averitt, X. Zhang, *Phys. Rev. Appl.* **2022**, *18*, 054086.
[47] X. Zhao, C. Chen, K. Kaj, I. Hammock, Y. Huang, R. D. Averitt, X. Zhang, *Optica* **2020**, *7*, 1548.
[48] H. Tao, A. C. Strikwerda, K. Fan, W. J. Padilla, X. Zhang, R. D. Averitt, *Phys. Rev. Lett.* **2009**, *103*, 147401.
[49] A. A. Basharin, V. Chuguevsky, N. Volsky, M. Kafesaki, E. N. Economou, *Phys. Rev. B* **2017**, *95*, 035104.
[50] L. Yuan, YY. Lu, *Opt. Lett.* **2017**, *42*, 4490.
[51] Y. Hu, M. Tong, S. Hu, W. He, XA. Cheng, T. Jiang, *Adv. Funct. Mater.* **2022**, *32*, 2203680.
[52] W. Suh, Z. Wang, S. Fan, *IEEE J. Quantum Electron.* **2004**, *40*, 1511.